

Large-scale volumetric flow measurement in a pure thermal plume by dense tracking of helium-filled soap bubbles

Huhn, Florian; Schanz, Daniel; Gesemann, Sebastian; Dierksheide, Uwe; van de Meerendonk, Remco; Schröder, Andreas

DOI

[10.1007/s00348-017-2390-2](https://doi.org/10.1007/s00348-017-2390-2)

Publication date

2017

Document Version

Final published version

Published in

Experiments in Fluids: experimental methods and their applications to fluid flow

Citation (APA)

Huhn, F., Schanz, D., Gesemann, S., Dierksheide, U., van de Meerendonk, R., & Schröder, A. (2017). Large-scale volumetric flow measurement in a pure thermal plume by dense tracking of helium-filled soap bubbles. *Experiments in Fluids: experimental methods and their applications to fluid flow*, 58(9), Article 116. <https://doi.org/10.1007/s00348-017-2390-2>

Important note

To cite this publication, please use the final published version (if applicable). Please check the document version above.

Copyright

Other than for strictly personal use, it is not permitted to download, forward or distribute the text or part of it, without the consent of the author(s) and/or copyright holder(s), unless the work is under an open content license such as Creative Commons.

Takedown policy

Please contact us and provide details if you believe this document breaches copyrights. We will remove access to the work immediately and investigate your claim.

Large-scale volumetric flow measurement in a pure thermal plume by dense tracking of helium-filled soap bubbles

Florian Huhn¹  · Daniel Schanz¹ · Sebastian Gesemann¹ · Uwe Dierksheide² · Remco van de Meerendonk³ · Andreas Schröder¹

Received: 28 March 2017 / Revised: 13 June 2017 / Accepted: 27 June 2017 / Published online: 3 August 2017
© Springer-Verlag GmbH Germany 2017

Abstract We present a spatially and temporally highly resolved flow measurement covering a large volume ($\sim 0.6 \text{ m}^3$) in a pure thermal plume in air. The thermal plume develops above an extended heat source and is characterized by moderate velocities ($U \sim 0.35 \text{ m/s}$) with a Reynolds number of $Re \sim 500$ and a Rayleigh number of $Ra \sim 10^6$. We demonstrate the requirements and capabilities of the measurement equipment and the particle tracking approach to be able to probe measurement volumes up to and beyond one cubic meter. The use of large tracer particles (300 μm), helium-filled soap bubbles (HFSBs), is crucial and yields high particle image quality over large-volume depths when illuminated with arrays of pulsed high-power LEDs. The experimental limitations of the HFSBs—their limited lifetime and their intensity loss over time—are quantified. The HFSBs' uniform particle images allows an accurate reconstruction of the flow using Shake-The-Box particle tracking with high particle concentrations up to 0.1 particles per pixel. This enables tracking of up to 275,000 HFSBs simultaneously. After interpolating the scattered data onto a regular grid with a Navier–Stokes regularization, the velocity

field of the thermal plume reveals a multitude of vortices with a smooth temporal evolution and a remarkable coherence in time (see animation, supplementary data). Acceleration fields are also derived from interpolated particle tracks and complement the flow measurement. Additionally, the flow map, the basis of a large class of Lagrangian coherent structures, is computed directly from observed particle tracks. We show entrainment regions and coherent vortices of the thermal plume in the flow map and compute fields of the finite-time Lyapunov exponent.

1 Introduction

Time-resolved volumetric flow measurements, using methods such as tomo-PIV (Elsinga et al. 2006), 3D PTV (Maas et al. 1993; Malik et al. 1993) or Shake The Box (Schanz et al. 2013b, 2016a), are typically restricted to relatively small volume sizes of the order of $\leq 200 \text{ cm}^3$ (Scarano et al. 2015). This limitation stems from the small size of commonly used seeding material, to accurately follow the flow (diameter range around $\sim 1 \mu\text{m}$ in air, 10–50 μm in water). Currently available high-repetition rate laser systems, which are typically used as a light source, do not provide enough intensity to allow for illumination of larger volumes, even for the larger particles used in water experiments. However, seeding particles whose density approaches that of the medium can be of larger size, while still accurately being able to follow the flow (Melling 1997). In line with this thought, neutrally buoyant helium-filled soap bubbles (HFSBs) have been used in air to allow for large-scale flow measurements in the laboratory. Applications range from traceline visualizations (Pounder 1956) over large-scale 2D-PIV measurements (Müller et al. 2000; Bosbach et al. 2009) to three-dimensional tracking of single bubbles

Electronic supplementary material The online version of this article (doi:10.1007/s00348-017-2390-2) contains supplementary material, which is available to authorized users.

✉ Florian Huhn
florian.huhn@dlr.de

- ¹ Institute of Aerodynamics and Flow Technology, Department of Experimental Methods, German Aerospace Center (DLR), Bunsenstr. 10, Göttingen, Germany
- ² LaVision GmbH, Anna-Vandenhoeck-Ring 19, Göttingen, Germany
- ³ Department of Aerospace Engineering, Delft University of Technology, Kluyverweg 1, Delft, The Netherlands

(Klimas 1973) and large-scale tomographic PIV of a convective flow (Kühn et al. 2011). Recently, a feasibility study demonstrated that HFBSs are a promising seeding material for low-speed wind tunnels (Scarano et al. 2015).

At the uppermost end of the range of large measurement volumes, open air experiments in the atmospheric boundary layer reach spatial scales of tens of meters, using, for example, snow particles as seeding material illuminated with a searchlight (Hong et al. 2014) or centimeter-sized fog-filled soap bubbles illuminated by the sun (Rosi et al. 2014). These studies show promise as techniques for real-size flow measurements behind wind turbines, but are of minor applicability in a controlled laboratory environment. Some of the previous particle tracking experiments with HFBSs in the laboratory examined large measurement areas (Klimas 1973; Biwole et al. 2009), but were limited in particle number, often tracking only a few tens or hundreds of bubbles. The largest investigated volume that allowed the description of instantaneous flow structures was applied by Kühn et al. (2011). A convection cell with a volume of approximately 56 L was investigated with two-pulse tomo-PIV. However, a large interrogation window size had to be chosen ($48 \times 48 \times 24$ mm), limiting the spatial resolution to large structures. In the first application of HFBSs for a wind tunnel experiment, Scarano et al. (2015) have shown that for higher flow speeds (~ 30 m/s) the production of enough bubbles to achieve a sufficient particle concentration within the measurement volume is a major issue. Due to the limitations in bubble number and due to the limits of the high-speed laser used for illumination, the volume size was restricted to 4.8 L in this experiment and the interrogation windows for a tomo-PIV analysis were large ($96 \times 96 \times 86$ voxels). In a follow-up paper, the same group reaches a measurement volume of 12 L at a free stream velocity of 8 m/s. To increase the seeding density to a mean particle distance of ~ 10 mm, they present a piston-based seeding generator with an accumulation and release strategy (Caridi et al. 2016). At a free stream velocity of 5 m/s, Schneiders et al. (2016) present a 3D tomo-PTV measurement downstream of a surface-mounted low-aspect-ratio cylinder in an increased measurement volume of 6 L.

In this paper, we present an LPT experiment with helium-filled soap bubbles in a thermal plume with an unprecedented measurement volume of 560 L and a high spatial resolution (mean inter-particle distance $d = 13.0$ mm). The application of the Shake-The-Box (STB) algorithm allows for an accurate and time-effective reconstruction of particle paths at high seeding concentrations, providing dense velocity and acceleration fields of the flow. The experiment has been designed to apply STB LPT to a turbulent low-speed flow with a high seeding concentration of helium-filled soap bubbles. Since the seeding generator was limited to six seeding nozzles

at the time of the experiment, a closed flow chamber was chosen. The moderate thermal forcing of the flow allows for a precise control of the small flow velocity and the involved turbulent structures; this is in contrast, for example, to a fan that already induces complex turbulent structures on the blades. Hence, for the designed convection experiment with moderate velocities (0.35 m/s), the bubble production rate and the recording frequency are not limiting factors.

The paper is organized as follows. In Sect. 2, we present the experimental setup and in Sect. 3 we describe the data analysis. The results for the flow field are shown in Sect. 4. In Sect. 5, we present the results of a Lagrangian transport analysis in the thermal plume. Finally, Sect. 6 summarizes the results and discusses future perspectives of the measurement technique.

2 Experimental setup

2.1 Convection chamber

The experiments are performed in a cylindrical convection chamber with a height of 2.00 m and a diameter of 1.83 m (Fig. 1). The top and bottom plates are constructed of wood, the back wall is made of aluminum, and the transparent front window is acrylic glass of 1 mm thickness. Non-transparent parts of the floor, walls and ceiling are painted black or covered with black self-adhesive film, to avoid scattered light and improve the contrast of the particle images relative to the background. The convection chamber is accessible from the rear side through a door in the aluminum wall. The chamber is equipped with a circular perforated tube at the bottom to rinse it with pressurized air and remove seeding.

LED illumination enters through an acrylic glass window of 1 m diameter in the ceiling, covered with a circular passe-partout (0.75 m diameter) that determines the width of the cylindrical measurement volume. The convective flow is forced by a standard 1500 W electric hot plate ($D = 188$ mm diameter, *Silva Homeline EKS 2121*) that is placed a few centimeters below the measurement volume. It is covered by a black circular 250 mm diameter aluminum plate of 10 mm thickness that serves as a heat reservoir to keep the temperature constant over time. The circular hot plate is mounted on a support of ~ 0.4 m height above the floor and with a diameter of roughly 350 mm (Fig. 1b). The elevated position of the heat source allows for a vertical flow along the contours of the support toward the hot plate, feeding the thermal plume over the hot plate. As mentioned by Pham et al. (2005), the elevated position stabilizes the horizontal position and diminishes strong lateral oscillations of the thermal plume.

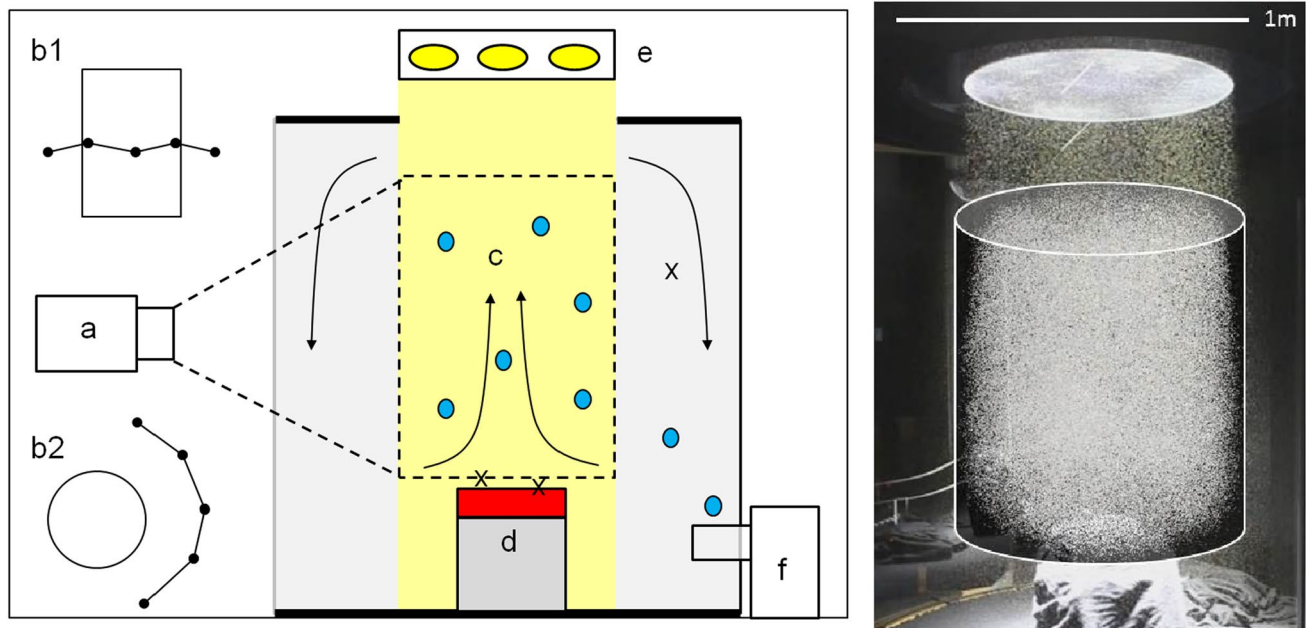


Fig. 1 (Left) experimental setup of convection chamber: (a) cameras; (b1, b2) front and top view of camera configuration; (c) field of view (FOV), (d) hot plate; (e) LED array; (f) bubble generator; (x) positions of three temperature sensors. (Right) photograph of the interior

of the convection chamber with elevated heat source in the center and illuminated HFSB. In the cylindrical measurement volume, the reconstructed 3D particle cloud is shown as an overlay

Before conducting experiments, the hot plate is heated up for a few seconds to reach the desired temperature. After waiting for some minutes, a uniform temperature distribution over the hot plate is attained. Three temperature sensors (thermocouples *Omega 5SC-TT-KI-40-1M*, AD converter *Labjack T7 Pro*) are installed in the convection chamber to monitor the temperature of the heated aluminum plate, the air temperature 2 mm above the plate as a proxy for the maximum air temperature, and the ambient air temperature outside of the plume (see Fig. 1 for positions of sensors). We also measure the temperature in the laboratory and observe that during the experiment no measurable increase of the temperature inside the convection chamber compared to the laboratory can be observed (cf. Fig. 2). The accuracy of the absolute temperature measurement is estimated to be ± 2 °C, while the relative temperature differences, relevant for the convective flow, are accurate within ± 0.5 °C. During the experiments, heat is provided by the aluminum plate, while the temperature of the hot plate decreased by less than 0.5 K (cf. Fig. 2).

2.2 Helium-filled soap bubbles

For LPT, the flow is densely seeded with neutrally buoyant HFSBs of 300 μm diameter. They are produced by a bubble generator prototype of *LaVision GmbH*, based on the orifice-type nozzle design discussed by Okuno et al. (1993) and used by Bosbach et al. (2009). A nozzle consists of

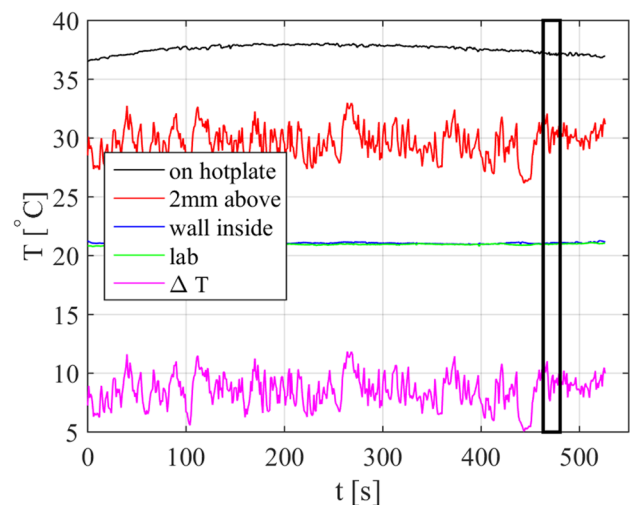


Fig. 2 Temperature log for the different temperature sensors. Measurement time window is marked by the black rectangle. ΔT is the temperature difference between air 2 mm over the hot plate and ambient air

three concentric channels—providing helium, soap solution (*ASAI 1035, Sage Action Inc.*), and pressurized air, from the center outward. It is covered by a cap with a small circular orifice. The two inner channels produce a thin helium-filled soap tube that is transported through the orifice by the surrounding air flow, subsequently breaking up into a single chain of equal-sized bubbles in the increasingly turbulent

air flow (see Fig. 3). Six nozzles are operated in parallel with a bubble production rate of $\sim 45,000/\text{s}$ each. This production rate is estimated from high-speed camera images at the outlet of the nozzle. The nozzles are directly placed at the bottom inside the convection chamber to enable a high seeding density in the large volume. HFSBs are injected vertically close to the wall to avoid the influence of the momentum of the nozzle jets toward the center where the hot plate is located. Before an experiment, the chamber is seeded for 30 s to reach a high particle concentration. A waiting period of around 135 s follows, to reach a homogeneous spatial distribution of the seeding and to let the motion induced by the nozzle jets decay. We adjust the neutral buoyancy of the HFSBs by varying the flow rate of helium, such that, by visual inspection, a zero settling velocity is attained in calm air. Careful experiments by Scarano et al. (2015) show that HFSBs follow the air flow at high accelerations of $\sim 10^4 \text{ m/s}^2$ in a wind tunnel even for a variation of the helium flow rate by a factor of two. Since in our convective flow, accelerations are much smaller ($a \sim 0.1 \text{ m/s}^2$ see results of LPT), we expect the tracer to be able to closely follow the air flow.

Soap bubbles burst, such that the lifetime can be a limiting factor, especially for large convective flows that are typically slow and involve long time scales. Bosbach et al. (2009) estimate the lifetime of HFSBs to be 1–2 min under similar conditions as in this experiment, e.g., room temperature and presumably relatively low relative air humidity in a laboratory. Here, we further quantify the full lifetime distribution of HFSBs at these conditions, $T = 21 \text{ }^\circ\text{C}$ and relative humidity of $\text{rh} = 37\%$, considering a simple population model approach. The convection chamber is considered to be a well-mixed box with uniform seeding density, experimentally brought about by strong mixing with a continuously running fan. The number of HFSBs in the convection chamber is assumed to evolve as

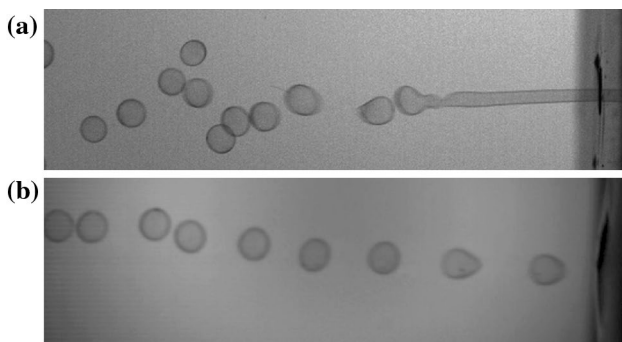


Fig. 3 High-speed images of the nozzle of the bubble generator. **a** Unstable working conditions with visible external breakup of the soap tube. **b** Stable working conditions where the soap tube breaks up internally and equally sized soap bubbles are produced

$$\frac{dN}{dt} = p(t) - d(t), \quad (1)$$

with the production rate $p(t)$ and the death rate $d(t)$. The production rate $p(t)$ is a step function, controlled by switching on and off a single nozzle of the bubble generator. The death rate is given by

$$d(t) = \int_{-\infty}^t p(t - \tau) \rho(\tau) d\tau, \quad (2)$$

with the probability density function of the lifetime $\rho(\tau)$, i.e., the death rate is given by integrating over all production rates in the past, weighted with the lifetime distribution. During the experiment in which the HFSB's lifetime is estimated, the particles are constantly produced with a single nozzle for 10 min, after which the production is switched off and images are acquired at a frequency of 1 Hz for a further 10 min. The number of HFSBs in the measurement volume $N(t)$ is determined by a particle detection algorithm applied to the images of the center camera. It turns out that $N(t)$ is well fit by the model when assuming $\rho(\tau)$ to be a Weibull distribution,

$$\rho(\tau) = \frac{k}{\lambda} \left(\frac{\tau}{\lambda}\right)^{-1} \exp\left[-\left(\frac{\tau}{\lambda}\right)^k\right], \quad (3)$$

with the scale parameter λ and the shape parameter k . The lifetime of soap films has been reported to follow a Weibull distribution with increasing decay rate due to an aging process (Gilet et al. 2007; Tobin et al. 2011).

Figure 4a shows the evolution of the particle number in the convection chamber and the fit function $N(t)$ obtained by integrating Eq. (1). The number of detected particles has a small dependence on the chosen intensity threshold; the curve in Fig. 4a is for a threshold of 150 gray value counts of the *pco.edge* sCMOS camera. It is expected that after an initial increase of the particle number, a plateau is reached, when production rate and death rate are equal with opposite signs such that the net change in particle number is zero. In Fig. 4a, a slight decrease of the plateau can be seen; this may be due to a non-constant production rate of the nozzle or inhomogeneous bubble quality, leading to earlier bursting of the initial bubbles. For the fit of the model to the data, data from $t \in [400, 620] \text{ s}$ is excluded, leading to a better fit in the initial rise and the final decay of the curve. The blue curve in Fig. 4b shows the lifetime distribution $\rho(\tau)$ for the best fit. Curves for other intensity thresholds in the particle detection, 100 and 200 counts, are also shown. According to this Weibull distribution, the mean lifetime of HFSBs is $\tau = 97 \text{ s}$ which confirms the rough estimate of Bosbach et al. (2009). Beyond a simple mean lifetime value, the complete lifetime distribution shows that the lifetimes of HFSBs are widespread with a long tail, explaining

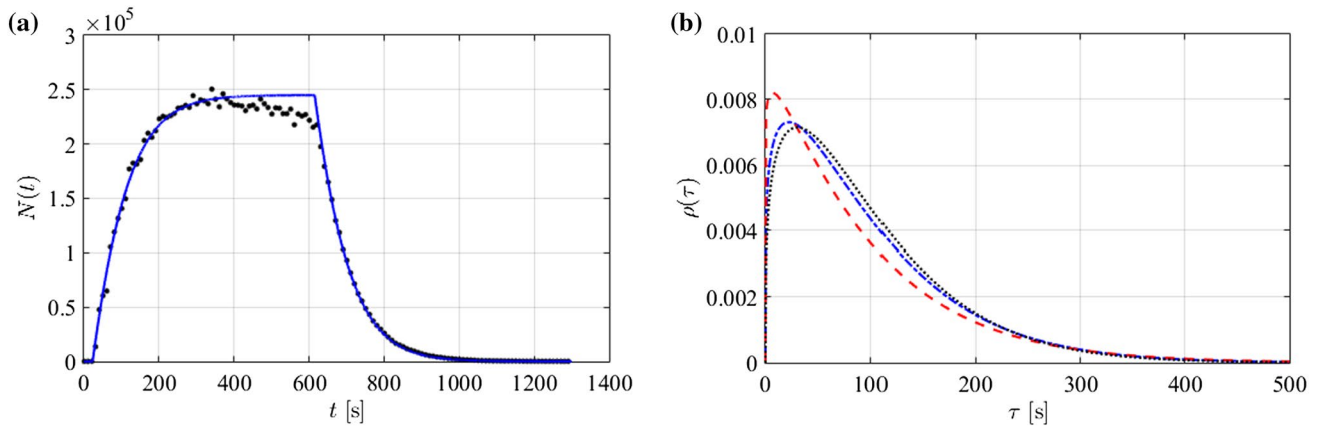


Fig. 4 **a** Temporal evolution of particle number $N(t)$ (dots) and optimized fit of the model Eqs. (1–3) (blue line). **b** Weibull distribution HFSB lifetime for intensity thresholds of 100 (red, dashed), 150

(blue, dashed dotted), and 200 counts (black, dotted). Parameters of blue curve: Shape parameter $k = 1.19$, scale parameter $\lambda = 103$ s, mean lifetime $\tau = 97$ s, standard deviation $\sigma_\tau = 82$ s

the observation that even after times as long as 5 min some HFSBs still remain.

Due to their large size, the intensity of the HFSB’s particle images is high in the experiment (Fig. 5). Beyond their limited lifetime due to bursting, however, one also has to consider a significant intensity loss over time. The mean intensity decays to half the initial value in 10 min. Figure 5a illustrates this intensity loss as a mean over the whole ensemble of particles. In an experiment with an initial impulsive seeding for only 2 s and low resulting seeding density, the intensity of individual particle images was determined and averaged over the measurement volume. The number of particles (blue curve) also decays,

diminishing the size of the particle ensemble with practically vanishing particle number after 700 s. Figure 5b shows the full intensity distributions of HFSBs that narrow and shift to lower intensity with increasing time.

Shrinking of the HFSBs is a possible aging process responsible for the intensity loss, as helium diffuses out of the bubble. Another process that we observed qualitatively is the shift of the reflected spectrum toward smaller wavelengths. To the eye, old HFSBs appear bluish in contrast to the reddish fresh HFSBs. A thinning of the bubbles skin with time could be responsible for this spectral effect. The detected intensity would consequently be lower, since the camera’s quantum efficiency curve drops quickly

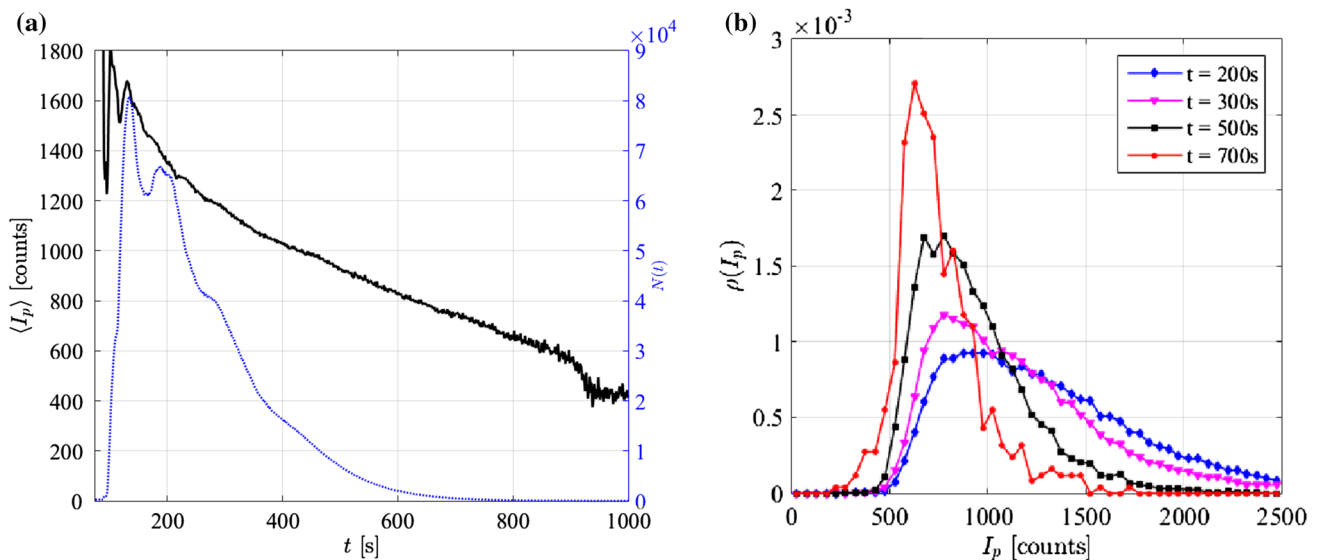


Fig. 5 Intensity loss of aging HFSB. **a** Decay of mean intensity of HFSBs (black, solid) and number of particles (blue, dotted) in an experiment with impulsive initial seeding for 2 s. **b** Probability distributions of particle intensity evolving with time

toward smaller wavelengths. Apart from aging processes, the quality of the soap solution influences the properties of the HFSBs. During the measurement campaign, the soap solution seems to change over time leading to less intense HFSBs. A thorough quantitative investigation of the physical reasons for the mentioned effects would require a specially designed experiment and is beyond the scope of this work.

In conclusion, given the time scales in the lifetime distribution and in the intensity loss, HFSBs can be recommended for measurements not lasting longer than ~ 2 min after bubble injection. For longer times, a continuous seeding is necessary to maintain the seeding density and the image quality. Before measurements, old and possibly recycled soap solution should be replaced by fresh solution.

2.3 LED light source

The measurement volume is illuminated by a white LED array consisting of seven standard collimated LED spotlights (*Treble-Light, Power LED 20000*) with an opening angle of 9° and 18,000 lm luminous flux at 170 W nominal electric power input each. One spotlight consists of 48 LEDs with 3.5 W each. The LED array is located 1 m above the ceiling of the convection chamber and a passe-partout of 0.75 m diameter on the ceiling window defines the cylindrical measurement volume. In the experiment, the LED light source is synchronized with the camera system and is pulsed with a period of 3 ms at 29 Hz, corresponding to a $\sim 10\%$ duty cycle.

As a reference, we measure the horizontal profile of the continuous light intensity (light meter, *Extech HD450*) at

the bottom of the convection chamber (red curve, Fig. 6) and at a height of 1.10 m across the measurement volume (blue curve). The illuminated volume is well defined by a sharp decay in light intensity, which helps to avoid light scattering from particles outside the measurement domain. Due to the opening angle of the collimated LEDs of 9° , the illuminated region is widened from 75 cm at the top window to around 80 cm in the measurement volume. An intensity dip in the center can be attributed to inhomogeneous distribution of LEDs in the light source and variations of intensity output between different LED arrays. Overall, the intensity of approximately 4.5×10^4 lx corresponds to $\sim 17,000$ lm over the whole area. A complementary view of the light intensity distribution is given in Fig. 6b, which depicts a 2D ensemble average of the intensity of all particle as identified by the STB particle tracking (see Sect. 3) over a run of 500 images. The x - and z -directions of the measurement volume were discretized in 2×2 -pixel bins and all particles located within such a bin are averaged, thus averaging over the streamwise y -direction of space. The different intensity of the LED spots can be seen. The spot located at $x = 200$ mm, $z = 200$ mm appears to have nearly double the intensity of the weakest one, located at $x = -200$ mm, $z = 200$ mm. Possibly, the inhomogeneities are due to different types of LED arrays and different cable lengths in the experiment. On one hand, these findings document that great care should be taken before assembling the illumination arrays to achieve homogenous lighting conditions. On the other hand, the flow measurement results below indicate that the STB particle tracking algorithm can handle even the present inhomogeneities in the illumination. In sensitive cases, pretesting with the STB would also allow for a direct assessment of the three-dimensional intensity field

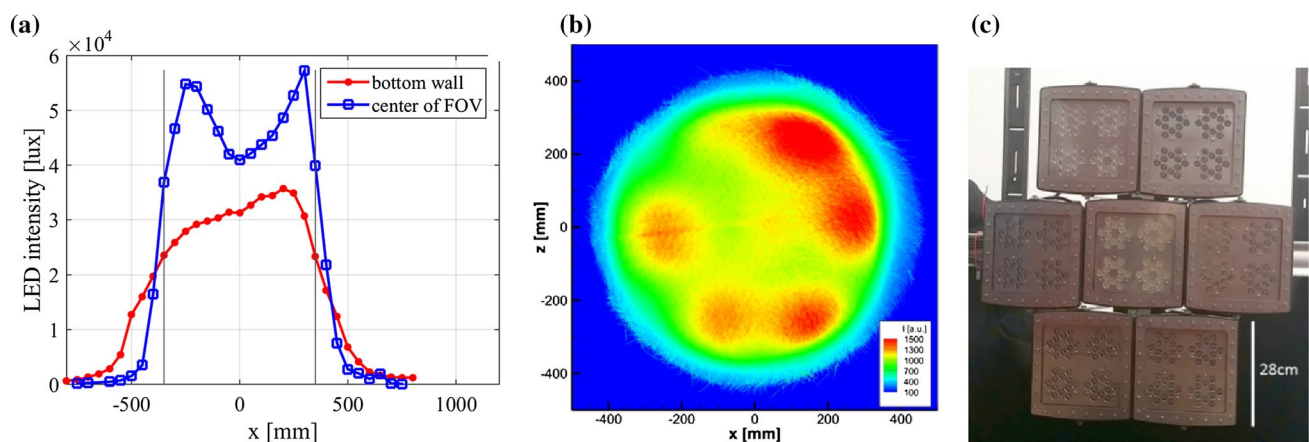


Fig. 6 **a** Intensity profile of continuous LED illumination across the measurement volume at a height of 110 cm (*blue squares*) and at the bottom of the convection cell (*red dots*) in the continuous mode. *Black bars* indicate the position of the passe-partout. **b** Horizontal

profile of particle intensity as given by LPT results, averaged over streamwise (y) direction. **c** White LED array composed of seven LED lights with 48 3.5 W LEDs each

and an optimization of the illumination when setting up the experiment.

2.4 Camera system

The camera setup consists of five sCMOS cameras (*pco.edge 5.5 PCO*) with a resolution of 2560×2160 pixels ($6.5 \mu\text{m}$ pixel size). They are arranged in a flat M-configuration with a small height difference between neighboring cameras of 15 cm (see Figs. 1, 7). The cameras are placed on a circle around the convection chamber with a distance of 2.25 m to the vertical center line of the cylindrical measurement volume, whereby the cameras look perpendicularly through the front window. The lines of sight of the outermost cameras have an angle $>90^\circ$ allowing for an accurate reconstruction of the particle position in all dimensions. The cameras are equipped with $f = 35 \text{ mm}$ lenses (Zeiss Contax) with the aperture set to $F_\# = 11$, yielding sufficient depth of field to image the volume with 0.8 m diameter. The cameras are rotated by 90° , so their FOV has a width of 0.85 m and a height of 1.1 m to capture the vertically extended cylindrical volume.

The magnification is $M = 0.016$, corresponding to 0.4 mm/pix , such that the two glare points—reflections at two points of the soap bubble (Kühn et al. 2011; Scarano et al. 2015)—fall into one single peak of an isotropic circular particle image of ~ 3 pixel diameter. In general, the image quality is one of the best ever seen by the authors in comparable experiments. An example of the high image quality is given in Fig. 8, showing a detail of a sample run at low seeding density and random flow. The sum of five consecutive images is shown, documenting the uniformity in particle imaging—both between the different bubbles,

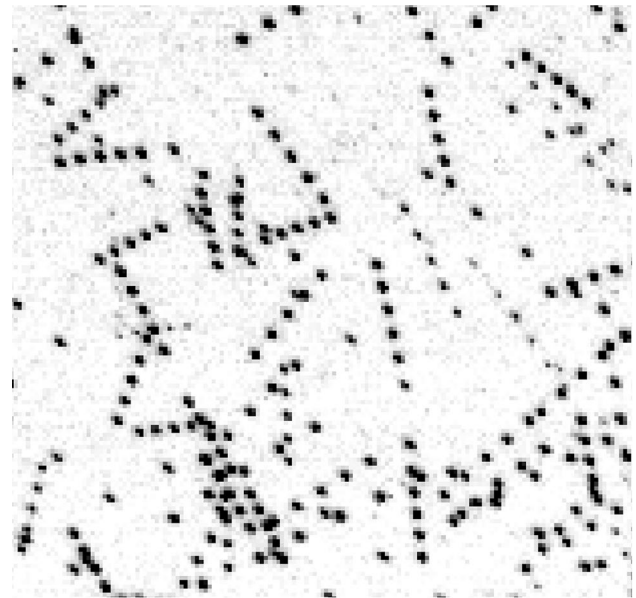


Fig. 8 Sum of five consecutive images at low seeding density with subtracted background (340 counts). Otherwise unprocessed camera image with inverted colors, showing the high quality of the HFSB's particle image

as well as in time for a single bubble. The high intensity of particle images due to the large diameter of the seeding particle ($300 \mu\text{m}$) and the absence of coherent light—preventing effects of interference or speckles—contribute to the image quality.

For the 3D calibration of the cameras, a large planar $950 \text{ mm} \times 760 \text{ mm}$ calibration target is placed vertically in the convection chamber and manually shifted to three positions, each 200 mm apart. Image acquisition, synchronization of cameras and the light source were

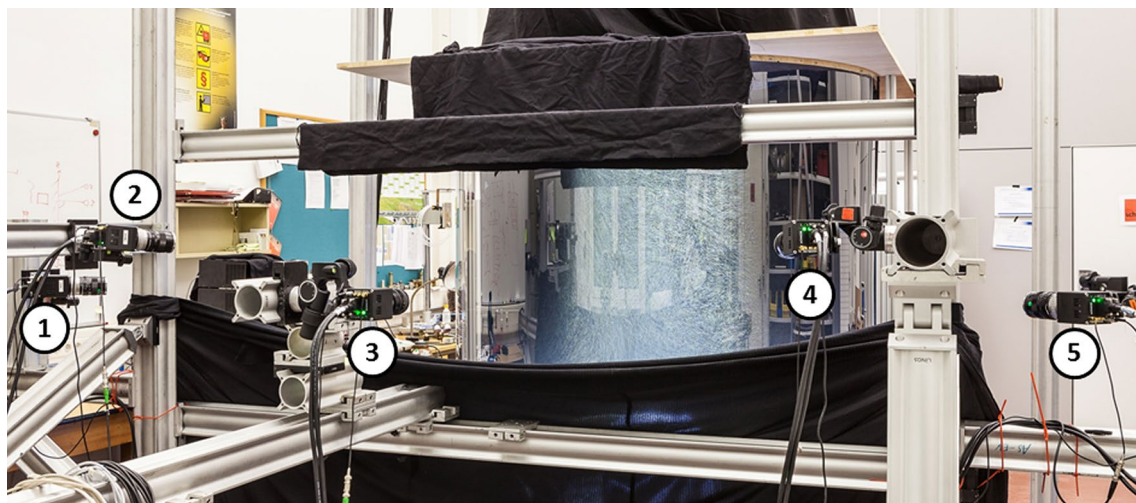


Fig. 7 Camera setup with five sCMOS cameras *pco.edge* around the convection cell. HFSB seeding in the convection cell appears white

controlled through the *DaVis*8.3 software (*LaVision*). The accuracy of the volumetric calibration was enhanced using Volume-Self-Calibration (Wieneke 2008); the particle imaging was calibrated, yielding a volumetrically resolved optical transfer function (OTF, Schanz et al. 2013a). All five cameras were connected to a single PC and the data were recorded directly to the hard disc. The recording frequency of 29 Hz reflects the maximum write rate that was attainable. Connecting each camera to a single PC would allow for a repetition rate up to 100 Hz at full frame resolution.

3 Data evaluation

For this study, a single measurement run with high particle density and large particle shift was chosen from the available material. The objective here is to assess the performance of the DLR STB algorithm under these conditions. The seeding density was found to be 0.08 ppp in the center of the image (Fig. 9). The temperature difference between the air directly over the hot plate and the surrounding air was approximately 8 °C (Fig. 2), leading to maximum velocities of around 0.35 m/s, and a maximum particle shift of nearly 30 pixels. 1000 images were recorded at a frequency of 29 Hz, of which 500 were evaluated using STB. Image preprocessing consisted of subtracting the spatially smoothed minimum image and a constant of 50 counts.

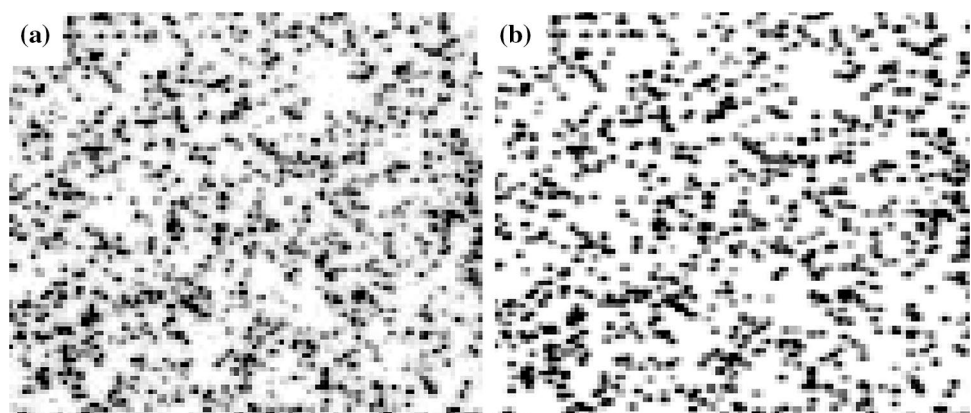
3.1 Shake-The-Box processing

The DLR in-house STB algorithm was applied. The main novelty of the LPT algorithm is to predict particle positions in the next time step by extrapolating already existing trajectories. By this procedure, the positioning problem and the problem of attaching particles to the right trajectory is greatly simplified. For details of the method, please refer to (Schanz et al. 2013b, 2014, 2016a). The following parameters were applied to the current dataset: The

number of triangulation iterations was set to 2—using an allowed triangulation error of 1.0 pixel—followed by one triangulation iteration using a reduced set of cameras. Each of these was followed by five shake-iterations [$n_1 = 2$, $n_2 = 1$, $m = 5$, $\varepsilon = 1.0$; see (Wieneke 2013)]. For the initialization phase (the first four images), the number of triangulations was doubled. No help of a predictor in form of a vector field gained by tomo-PIV processing was used in this case. As shown in Fig. 10a, the number of tracked particles quickly increases with the number of processed images. After the initialization phase, around 53,000 tracks of length four are found. This number rises to 110,000 only three time steps later and reaches 200,000 at time step 18. For this first pass (going forward in time), the number of tracked particles saturates at just over 250,000 after about 80 images. From there on, the tracked particle number decreases, as bubbles burst and disappear from the tracking system. When reaching the end of the time series, time is reversed and the algorithm walks backwards in time through the dataset. By doing so, known tracks that were not immediately found within the first pass are extended and the first time steps, where the tracking system was not yet converged in the first pass, are completely reconstructed. At the maximum, around 275,000 particles are simultaneously tracked in the second pass. To the knowledge of the authors, this is an unprecedented number for particle tracking methods, which typically operate with hundreds or a few thousand particles within the same image.

Figure 9 compares the camera image to the virtual image, created by reprojecting all tracked particles. The high quality of the tracking process is documented in Fig. 10b, which shows the statistics track length after pass 2. A distinct peak can be seen at 500 images, showing that over 81,000 particles have been tracked over the whole time series. These are particles slowly moving downwards in the recirculation region. The rest of the tracks have lengths that are evenly distributed, reflecting the fact that many particles are transported at different speeds into

Fig. 9 **a** Details of camera image. **b** Reprojection of particle distribution as reconstructed by STB



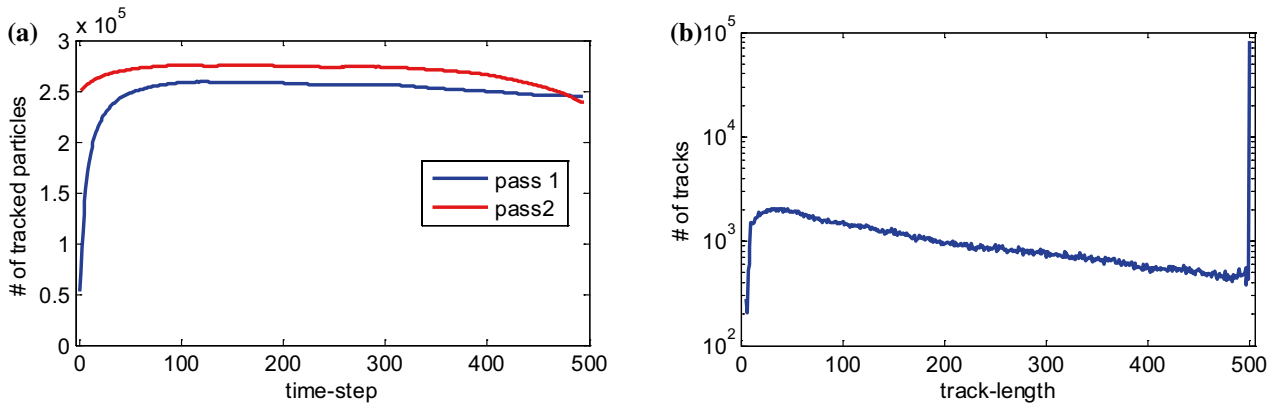


Fig. 10 **a** Development of number of tracked particles over time for both passes of STB. **b** Statistics of track length after pass 2

and out of the volume. The computational effort, combined for both passes, is around 220 s per time step on a 16-core Xeon server. A recently optimized version of the STB code further reduced this time to around 40 s for two passes on a 4-core i7 desktop computer.

Following the second pass, the particle tracks are fitted with a cubic B-spline curve with the TrackFit algorithm (Gesemann et al. 2016). On average, the particles are moved by 0.103 px from their original position (0.046 px in x -, 0.040 px in y - and 0.083 px in z -direction). The velocity values and acceleration values are calculated as derivatives of the B-spline curve. After fitting, a particle position accuracy of $\sim 36 \mu\text{m}$ (0.086 px) and a velocity uncertainty of $\sim 0.4 \text{ mm/s}$ is estimated from the spatial spectrum of the tracks; this corresponds to a dynamic velocity range of $\sim 875:1$.

4 Flow field results

4.1 Mean field and velocity profiles

Based on a recording of 1000 consecutive time frames at a lower seeding concentration ($\sim 42,000$ particles), the mean field of axial velocity is obtained by bin averaging the scattered velocity data. For the lower seeding concentration, a longer time series is available with potential advantages for the convergence of the statistics. Despite the relatively poor convergence of the statistics, some basic properties of the mean field can be observed and compared to another experiment (Pham et al. 2005). Figure 11a shows the radially averaged axial velocity. Directly above the heat source, fluid is accelerated by the buoyancy force, reaching a maximal axial velocity at $y^* = y/D \sim 1.5$. At larger y^* , axial momentum increasingly diffuses into the lateral quiescent

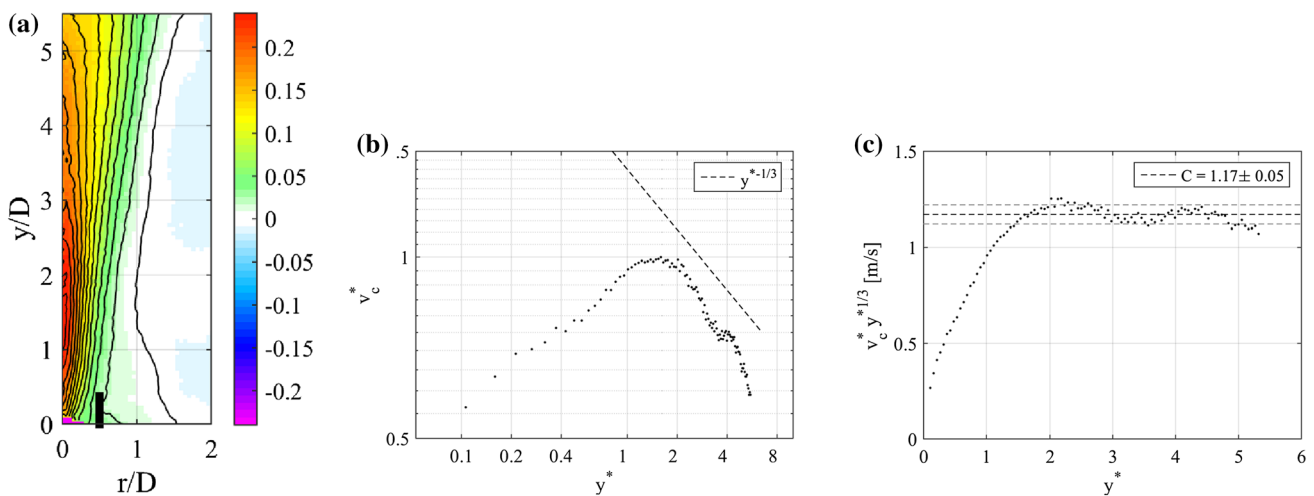


Fig. 11 **a** Mean axial velocity [m/s] averaged in circular bins with radius r . Contours are 0.02 m/s apart. *Black bar* indicates extension of the heat source. **b** Central profile of axial velocity v_c^* along

the plume axis (circular bin with radius 0.1 D) with turbulent scaling regime. **c** Compensated axial velocity profile

fluid and the central axial velocity decreases. Figure 11b shows the axial velocity along the central axis of the plume. A simple box model of the plume assuming conservation of volume, momentum and density deficiency (equivalent of heat) (Morton et al. 1956; Pham et al. 2005; Plourde et al. 2008) leads to an expected $-1/3$ power scaling of the decaying axial velocity at the center $v_c^*(y^*) = Cy^{*1/3}$, where v_c^* is the axial velocity at the center normalized to its maximum. We observe an early initiation of the $-1/3$ scaling at $y^* \sim 2.0$ (Fig. 11b), equivalent to a fully turbulent plume. This is earlier than the transition at $y^* \sim 4$ reported by the experimental study of Pham et al. (2005). In their setup, the heat source is coplanar with the bottom wall, while in our setup, it is located on a support of height $\sim 2D$. Thus, air is entrained into the plume laterally from below the heat source and the inward flow around the edges of the heat source already generates turbulent instabilities, leading to earlier onset of turbulence. With a value of $C = 1.17 \pm 0.05$ (Fig. 11c), the involved constant is somewhat smaller than the value of 1.26 reported by Pham et al. (2005).

4.2 Acceleration statistics

The acceleration of particles decorrelates faster than the velocity and therefore statistics show a better convergence for the same data base of 1000 consecutive frames. Figure 12 shows the mean fields of acceleration in the thermal plume averaged in circular bins. With a bin size of 10 mm, most bins comprise between 10^3 and 10^4 data points, with only the central region having a number of data points below 10^3 . While the mean of horizontal acceleration, $\langle a_x \rangle$ and $\langle a_z \rangle$, vanishes, the buoyancy force in positive y -direction is clearly apparent in the mean field of the vertical acceleration $\langle a_y \rangle$. The maximal value of $a_y = 0.12 \text{ m/s}^2$ is reached at $y/D \sim 0.5$. This mean vertical acceleration corresponds to a mean temperature difference of $\langle \Delta T \rangle = T_0 \langle a_y \rangle / g \sim 3.6 \text{ K}$ (cf. Eq. 4), which seems realistic, given the temperature difference of 8 K between the heat source and the ambient air (cf. Fig. 2). A black bar at $r/D = 0.5$ marks the extension of the heat source at the bottom of Fig. 12b. The region of positive upward buoyant acceleration coincides with the edge of the heat source. The spatial distributions of fluctuations of acceleration are uniform for all three directions (Fig. 12d–f). Contours show a similar opening angle of the plume as the mean velocity field in Fig. 11a. The fluctuations of acceleration reach values of up to $\sim 0.12 \text{ m/s}^2$ at the center at $y/D \sim 2.5$. This maximal magnitude of fluctuations is similar to the maximal mean upward buoyant acceleration.

Figure 13 shows the probability density functions (pdfs) of acceleration at selected points in the thermal plume. The grid of reference points is marked in Fig. 12b. Each subfigure in Fig. 13 represents a set of pdfs along a vertical

column in the thermal plume ($y/D = [1, 2, 3, 4, 5]$) at a constant distance from the center ($r/D = [0, 0.5, 1.0]$), cf. Fig. 12b. The pdfs are plotted with a logarithmic y -axis. For a better overview, the normalized pdfs have been shifted by a constant factor of 10 and ordered such that the uppermost curves correspond to the uppermost point in the column. At the center ($r/D = 0$), the shift of vertical acceleration a_y toward positive values due to the buoyancy can clearly be seen, while the distributions in the two horizontal directions (x, z) have zero mean and are isotropic. Toward the top of the plume, the a_y -curve approaches the curves of the horizontal acceleration (a_x, a_z) and all three curves converge at the uppermost point, i.e., the developed turbulence leads to isotropic distributions of acceleration. At a distance from the center of $r/D = 0.5$, in the shear layer at the edge of the heat source, the standard deviation of the acceleration is smaller than in the center (Fig. 12e). However, higher extreme accelerations appear in the longer tails of the pdf (Fig. 13b). While the acceleration pdfs at the center follow closely a Gaussian distribution (bold black line in Fig. 13a, Gaussian distribution with standard deviation σ_{ax} and zero mean), in the shear layer the acceleration pdfs significantly deviate from a Gaussian shape. The distribution at the top of Fig. 13b shows an exponential decay. The horizontal acceleration pdfs in Fig. 13b fall on top of each other, while in the vertical acceleration (red curve), a positive mean value, i.e., a contribution of the buoyancy, can still be observed. At a distance from the center of $r/D = 1.0$, the acceleration pdfs are isotropic without any influence from the buoyancy forces. The non-Gaussian shape suggests that in the outer part of the thermal plume, the acceleration is dominated by turbulent motions (cf. e.g., La Porta et al. 2001; Rosi et al. 2014), i.e., by the pressure gradient.

4.3 Instantaneous flow results

Figure 14 shows an instantaneous flow situation depicted by $\sim 275,000$ particle tracks, whose velocity vectors are drawn for three consecutive time steps and color-coded by streamwise velocity. A front view and a top view of the entire measurement volume are provided. The convex hull around all particles has a mean volume of 560 L. A large region of slowly moving particles surrounds the rising thermal plume. Due to the confining boundaries of the convection cell, outside of the thermal plume the flow is slightly downwards on average. In the center of the plume, the maximum velocity values are $\sim +0.35 \text{ m/s}$. In the presented time instant, the plume is broadened in the z -direction, compared to the x -direction, despite the circular symmetry of the hot plate. Figure 15 focuses on a central slice of the particle trajectories, giving an impression of the spatial sampling of flow structures with the dense seeding.

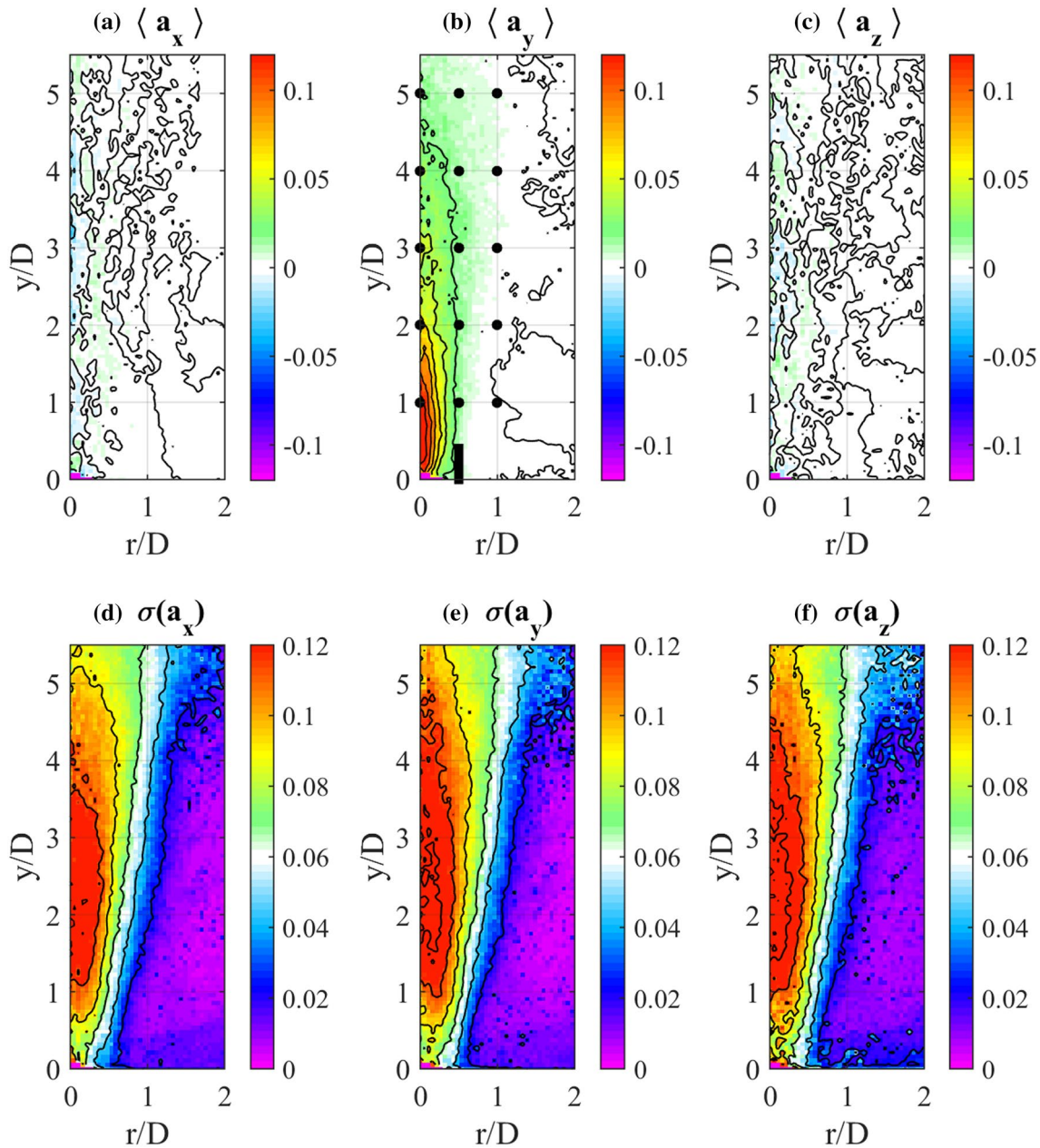


Fig. 12 **a–c** Mean and **d–f** fluctuations (standard deviation) of the particle acceleration. Bin size is 10 mm in both radial and vertical direction. Contours have a separation of 0.01 m/s^2

Locations of vortical structures can already be identified by looking at the particle tracks in Fig. 15; however, a quantitative description of vortices expressed as vorticity or using the Q-criterion would be desirable. To this end, the discrete Lagrangian information of velocity and acceleration at the scattered particle location is interpolated onto an Eulerian grid using the DLR in-house algorithm ‘FlowFit’ (Gesemann et al. 2016). In the FlowFit algorithm, the interpolating function is composed of a weighted sum of three-dimensional and evenly spaced cubic B-splines. To

determine the weights, the interpolant is fitted to the measured velocity and acceleration values at scattered particle positions using velocity and pressure as fit variables. In the most advanced version of FlowFit used here, a full Navier–Stokes regularization is implemented. The cost function of this optimization problem includes six terms: the difference between data points and the B-spline interpolant for (1) velocity and (2) acceleration (fit it data); the penalization of high wavenumbers of the (3) velocity and (4) pressure field (smoothing); (5) the penalization of

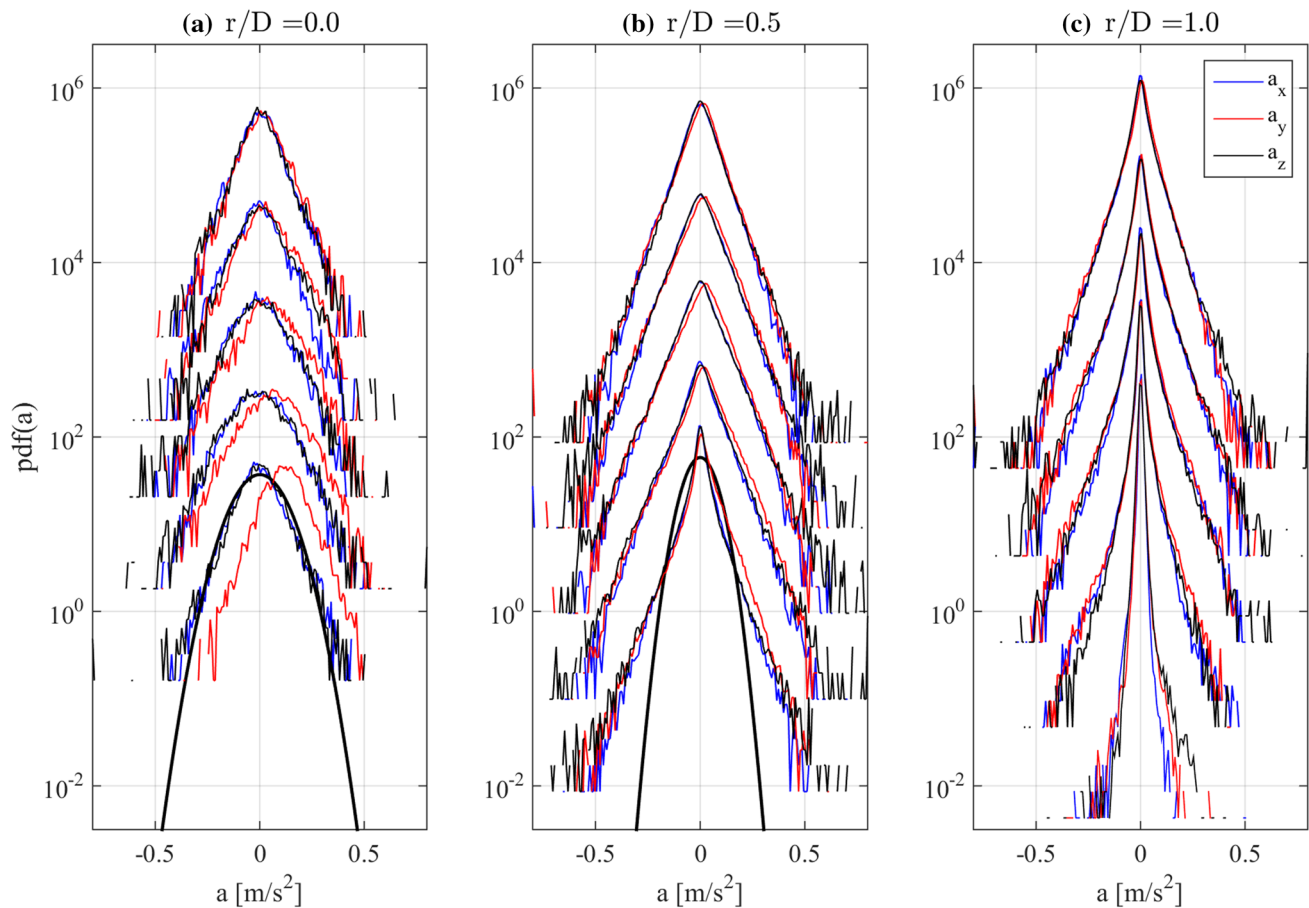


Fig. 13 Probability density functions of particle acceleration based on bin averaging over a circular bin with 50 mm width in both radial and vertical direction. The central position of the bins are ordered on a grid which is marked in Fig. 12b above. Pdfs are shifted such

that the lowest corresponds to $y/D = 1$ and the uppermost to $y/D = 5$. The number of data points is **a** $n \sim 7000$, **b** $n \sim 130,000$, **c** $n \sim 280,000$. **Bold black curves in a and b** are Gaussian distributions for comparison

divergence of the velocity field, $\nabla \cdot \mathbf{u}$ (incompressible); and finally, (6) the penalization of $\nabla \cdot \partial \mathbf{u} / \partial t$. The last term being zero translates to a simplified coupling of the velocity and the acceleration field through the material derivative. The material derivative introduces a non-linearity into the cost function, leading to a non-linear least squares problem which is solved with the L-BFGS method. Once the interpolant is computed, it can be sampled on a regular grid, including its first and second spatial derivatives that are analytically obtained from the B-splines. Vorticity or the Q-criterion can thus directly be computed without numerical differentiation. The FlowFit interpolation was applied to each of the 500 time steps, taking velocities and accelerations of the respective tracked particles as input data. The B-spline system is setup, such that on average ten B-spline cells are present for every particle (0.1 particles per cell), leading to a spacing of ~ 6 mm between the cells. The flow was assumed to be incompressible which is reasonable to first approximation, given the small temperature

differences in the flow. The L-BFGS algorithm is iterated until convergence and the resulting continuous function is closely sampled on a grid with 3 mm spacing, ultimately leading to volumes of $254 \times 334 \times 254$ vectors. On a single core processor, the FlowFit interpolation takes about 2 h per frame. Performing the FlowFit interpolation for several frames simultaneously is embarrassingly parallel.

An example of the results gained by applying FlowFit to the STB track data is given in Fig. 16, which shows isosurfaces of the Q-criterion for the same time step shown in Fig. 15. The full amount and extent of the vortical flow structures in the plume becomes apparent. Long, undisturbed vortices are identified in the shear layers surrounding the center of the plume. Central structures are smaller, but show equal strength. Movies of the temporal evolution of the plume are available in the supplementary data [link to Suppl. Data]. When looking at a time series of such images, a high temporal coherence is noticeable, i.e., isosurfaces evolve smoothly in time. The Q-criterion

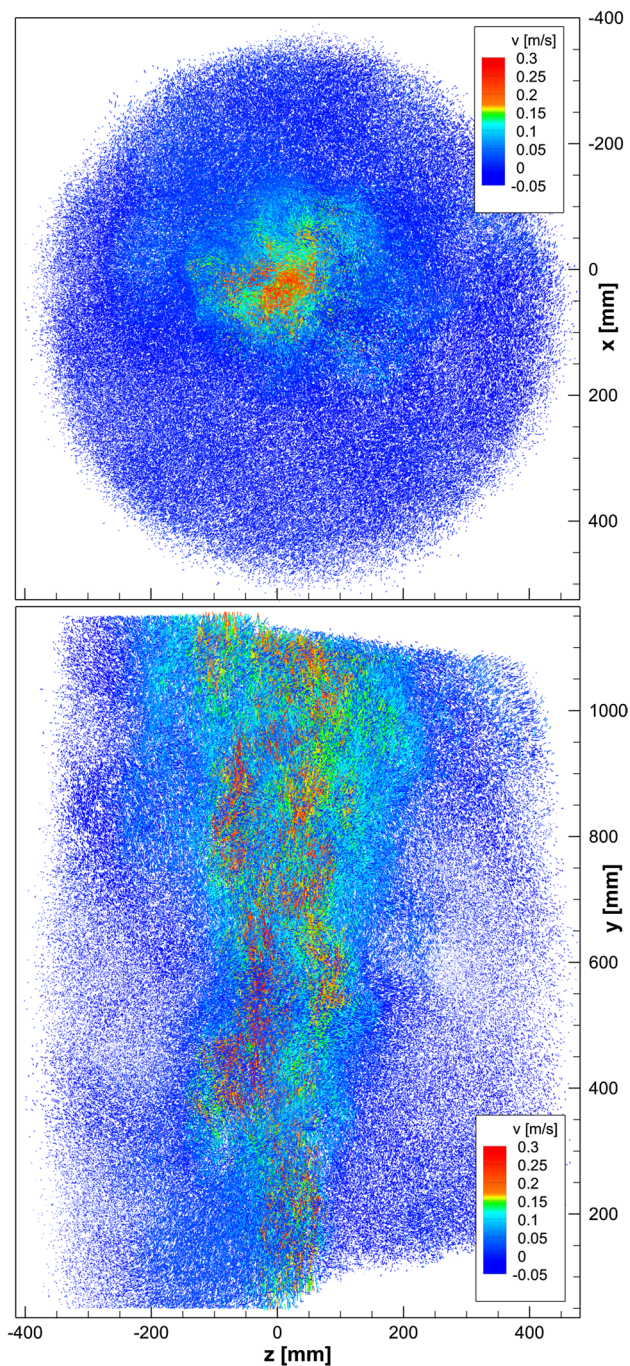


Fig. 14 Top view and front view of the entire measurement volume, showing $\sim 275,000$ particle tracks for three consecutive time steps, color-coded by streamwise velocity v . The inclined upper and lower bounds of the measurement volume (lateral view) are due to the opening angle of the cameras ($\sim 25^\circ$)

is derived from the velocity gradient tensor. As such, the temporal coherence is a clear indication that the LPT measurement at high seeding density in combination with the FlowFit interpolation strategy is able to recover the vast majority of the present flow structures. The high quality of

the tracking process translates directly into the quality of the Eulerian representation.

The high position accuracy in the reconstructed trajectories, which is achievable due to the high particle image quality, allows for an evaluation of the particle accelerations; these are the second temporal derivative of the trajectory. Figure 16 shows tracks that are color-coded by streamwise acceleration. The acceleration varies smoothly in the measurement volume. Around vortices oriented with their axis in x -direction (out of plane), the centrifugal acceleration of the circular motion can be observed.

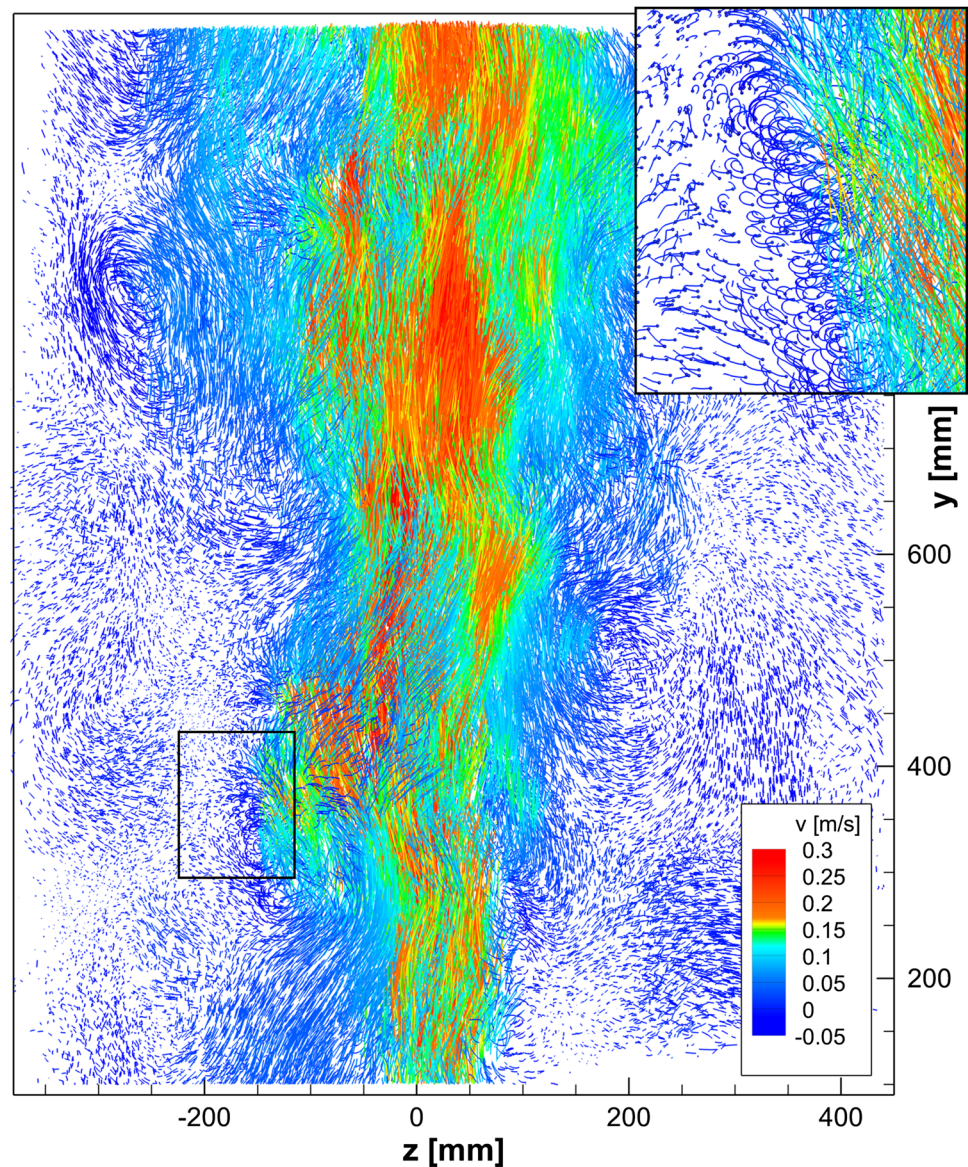
Just as for velocity, the acceleration can be interpolated onto an Eulerian grid using the FlowFit algorithm. Figure 17a displays an interpolation with only a smoothing constraint, but no further regularizations. The resulting field shows many isolated small structures that seem unphysical and point to a poor reconstruction of the acceleration field. In a strict sense, adding further regularizations to the interpolation is limited in the present flow by the unknown buoyancy term in the momentum equation (last term)

$$\rho_0 \mathbf{a} = -\nabla P + \mu \Delta \mathbf{u} - \rho_0 \mathbf{g} \Delta T / T_0, \quad (4)$$

written here in the Boussinesq approximation (e.g., Kundu and Cohen 2008). The viscous term is often neglected in turbulent flows, since it is small compared to the dominant pressure gradient term. If also the buoyancy term was negligible, the acceleration field would be curl-free and could be regularized with the condition of vanishing rotation. However, a rough estimation of the buoyancy term with $\Delta T = 2$ K, a typical temperature fluctuation at 100 mm above the heat source, gives a value of ~ 0.07 m/s² for the buoyancy acceleration. This acceleration is not small compared to the magnitude of the total measured acceleration of ~ 0.20 m/s². Maximal temperature differences directly above the heat source may be even as high as $\Delta T = 8$ K (cf. Fig. 2), making buoyancy locally the dominant term in the momentum equation close to the heat source.

Nevertheless, when neglecting the unknown buoyancy, a joint interpolation of the velocity and acceleration fields with the complete Navier–Stokes regularization (pressure and viscous force) leads to a reconstruction of the acceleration field that seems smoother and more physical (cf. Fig. 17a, b). Isolated pieces of the isosurfaces become connected and structures of positive and negative centripetal acceleration adjacent to vortices appear elongated, as expected (cf. Figs. 17b to 16). Why and where is the reconstruction improved when applying a physically incomplete regularization? The elongated vortices are located in the shear layer, where ambient air is entrained and the temperature difference is lower, leading to a small buoyancy force. Furthermore, in the rotating

Fig. 15 Particle trajectories with a length of 11 time steps in a central slice with 100 mm thickness, color-coded with vertical velocity. Detailed view (*upper right*) corresponds to the region in the *black rectangle* with 41 time steps in a slice of 40 mm thickness



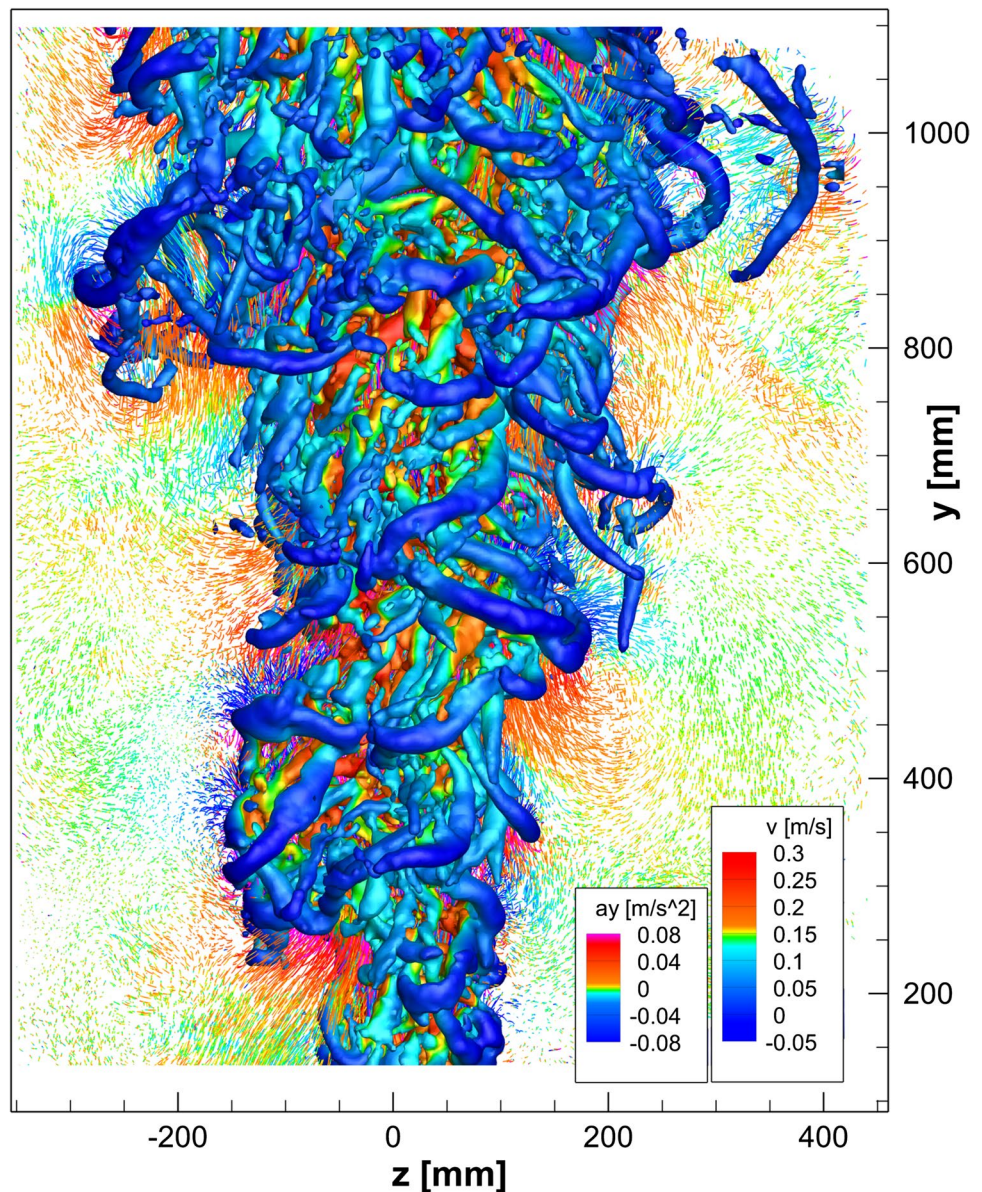
vortices, the centripetal pressure gradient force is strong. Therefore, applying the Navier–Stokes regularization without buoyancy improves the reconstruction of these vortex cores. In regions with a large buoyancy term, i.e., predominantly in central filamentous regions emanating from the heat source, the regularization without buoyancy might indeed bias the reconstructed acceleration field. Systematically investigating the local magnitude of the buoyancy force and the implications on the regularization scheme could be done on numerical data, but is beyond the intended scope of this paper.

In summary, the presented results demonstrate that detailed instantaneous fields of velocity and acceleration can be measured in large volumes when tracking HFSBs with the STB method.

5 Finite-time fluid transport and Lagrangian coherent structures

Flow measurements with the Lagrangian particle tracking (LPT) method STB for the first time offer a dense tangle of experimental particle trajectories that represent a direct measurement of the flow map. This flow map is the building block of the detection of a wide class of Lagrangian coherent structures (Peacock and Dabiri 2010; Peacock et al. 2015; Haller 2015). The following Lagrangian analysis of the experimental flow field is concerned with transport of fluid in space over finite times. In line with the Lagrangian frame of fluid motion, trajectories are tracked from an initial position at time t_0 to the final position at time $t = t_0 + T$ after a predefined time period T .

Fig. 16 Isosurfaces of Q-criterion (5 s^{-2}) color-coded by streamwise velocity and particle tracks (11 time steps, slice of 50 mm thickness) color-coded with streamwise acceleration



Properties of the fluid are advected along the trajectory, where the advective transport of heat, momentum and chemical tracers is of special interest in many applications. The key object for finite-time transport and the related Lagrangian coherent structures is the flow map $F_{t_0}^t(x)$ that maps initial fluid positions $x_0 = x(t_0)$ to their final position $x(t) = F_{t_0}^t(x_0)$ at a later time. Most flow data sets are given as a velocity field from experimental or numerical experiments, and the flow map must be computed by integrating $\partial_t x_p(t) = v(x)$ to obtain trajectories of fluid elements. With dense LPT, however, the flow map can directly be derived from measured trajectories. This idea was put forward by Raben et al. (2014) for two-dimensional flows and thereafter extended to

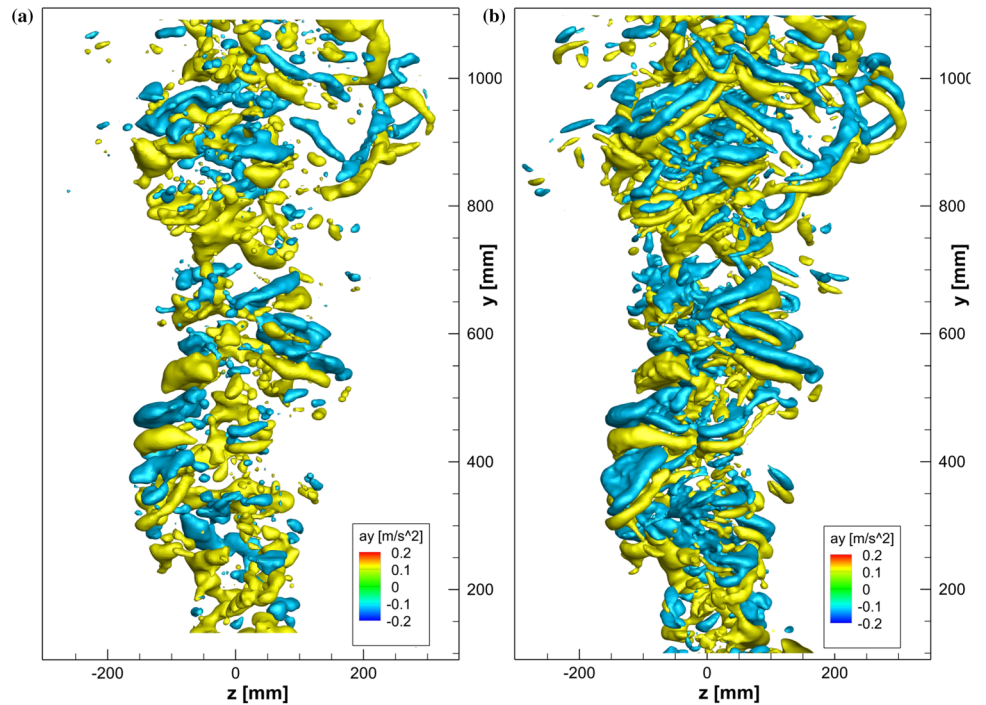
three-dimensional flows on unstructured grids by Rosi et al. (2015). In contrast to their work that focuses on simple vortical flows, the attainable spatial resolution of the flow map with the dense trajectory data in our experiment is significantly higher such that more complex flow structures can be represented. In the following example, we reconstruct a detailed flow map and analyze fluid transport in the thermal plume.

The flow map $F_{t_0}^t(x)$ is given as the concatenation of a series of Δt -flow maps

$$F_{t_0}^{t_n} = F_{t_{n-1}}^{t_n} \circ \dots \circ F_{t_0}^{t_1} \quad (5)$$

with the time period $t_i - t_{i-1} = \Delta t$ (Brunton and Rowley 2010), where the time increment Δt is the

Fig. 17 **a** Isosurfaces of streamwise acceleration ($a_y = \pm 0.12 \text{ m/s}^2$). Reconstruction of acceleration field with smoothness as only regularization. **b** Reconstruction with full Navier–Stokes regularization



temporal resolution of the measured particle trajectories, $\Delta t = 34.5 \text{ ms}$ in the experiment. The composed flow map $F_{t_0}^{t_n}$ covers the time period $T = n\Delta t$. A Δt -flow map is given only at particle positions x_p and must be interpolated to a regular grid by the interpolation operator I_x ,

$$F_{t_0}^{t_1}(x) = I_x x_p(x_p(t_0), t_1). \tag{6}$$

For this interpolation, we use the FlowFit routine described above. On the level of the flow map, incompressibility of the flow corresponds to the condition $|\det \nabla F| = 1$. This condition can be used for a regularization of the field,

in the case of poor spatial resolution. Here, for a densely seeded flow, we refrain from using this regularization.

For the analysis of the flow of the thermal plume, the flow map is computed backward in time. This approach is linked to the question where the fluid originates from. The flow map is constructed on a regular grid and fluid particles are tracked back to their origin. Figure 18 shows the flow map at a central section of the plume at $z = 0 \text{ mm}$. The original x -position of the fluid is shown in Fig. 18a, the original y -position is shown in Fig. 18b. The color-coded representation of original position can also be interpreted as the forward advection of particles carrying their original

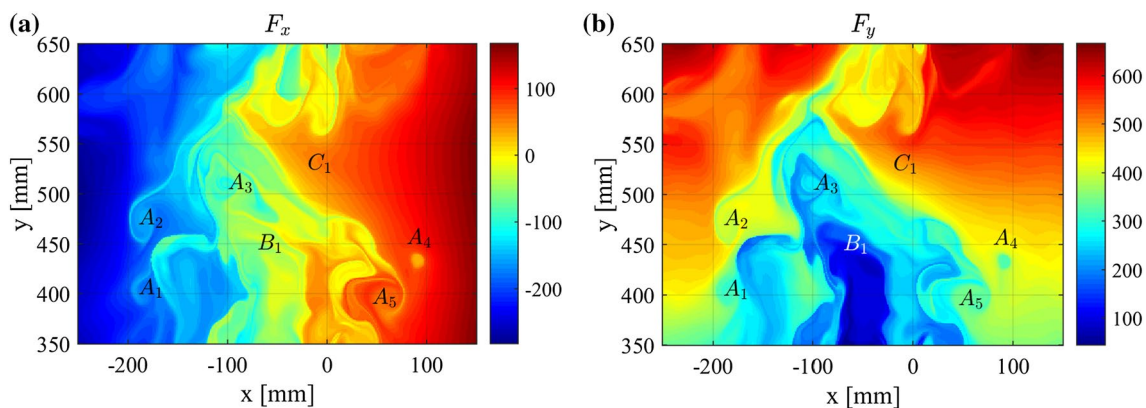


Fig. 18 Backward time flow map at $t_0 = 261, T = -35\Delta t$. Colors indicate where a particle—now located at position (x, y) —was at the earlier time $t = t_0 + T = 226$. Both spatial components F_x and F_y are

shown. **a** F_x -component with vortical structures (A_{1-4}), and a prominent lateral intrusion of air from the right (C_1). **b** F_y -component with vertical intrusion of air from below (B_1)

position at time $t = t_0 + T = 226$ to their new position at time $t_0 = 261$, with $T = -35\Delta t$. In the arising pattern, several distinct coherent structures can be identified. Several circular tracer patterns induced by vortices are marked with the letter A. The colors in Fig. 18 show, for example, that the small circular fluid region A_4 , now located at $(x, y) \approx (90, 440)$, was earlier located at $(F_x, F_y) \approx (50, 300)$. Hence, the fluid region originates from a lower, more central part of the plume. The vertical intrusion of air from below at the center of the thermal plume is characterized by low original y-position (Fig. 18b, blue, B1). Also lateral entrainment of air into the rising plume can be observed (cf. Pham et al. 2005, their Fig. 9). The region C_1 has high original x-position (Fig. 18a, orange/red), indicating that the fluid was drawn into the rising plume from the quiescent right side. These three coherent structures of finite-time mixing are relevant for the fluid dynamics of the plume, especially if they are combined with the momentum and temperature fields. Heat is transported from the thermal boundary layer of the hot plate upwards, and momentum is mixed laterally from the interior of the plume through the turbulent shear layer into the quiescent ambient fluid. This transport is not continuous in time but is generated by intermittent intrusions of air regions carrying the particular quantity which can be visualized by means of the flow map.

The deformation of the fluid over a predefined finite time gives rise to hyperbolic structures where fluid from different origins merge. These hyperbolic structures, a subclass of Lagrangian coherent structures (LCS) (Haller 2015), can be diagnosed from fields of the backward finite-time Lyapunov exponent (FTLE) (Haller 2001). The FTLE $\sigma(x, t, t_0)$ is a measure of stretching of the fluid over a finite time and is computed from the flow map $F_{t_0}^t(x)$ as

$$\sigma(x, t, t_0) = \frac{1}{|t - t_0|} \ln \sqrt{\lambda_{\max}(C_{t_0}^t(x))} \quad (7)$$

where $C_{t_0}^t(x) = \nabla F^T \nabla F$ is the Cauchy–Green strain tensor and λ_{\max} is its largest eigenvalue. Figure 19 shows the backward-time FTLE field with the typical elongated structures that separate fluid from different origins. According to its definition, the FTLE reaches high values along lines of high gradients of the flow map (cf. Fig. 18). With its units of 1/s, the FTLE represents an average separation rate between neighbored fluid elements over finite time in the direction of maximal stretching or shearing. According to their different origins, the patterns in the flow map in Fig. 18 are surrounded by lines of high FTLE values. Furthermore, lines of high FTLE values coincide with filamentary structures in the flow map, since filaments are characterized by a high stretching rate in one direction. In summary, the flow map constructed purely from dense experimental trajectory data from our flow measurement

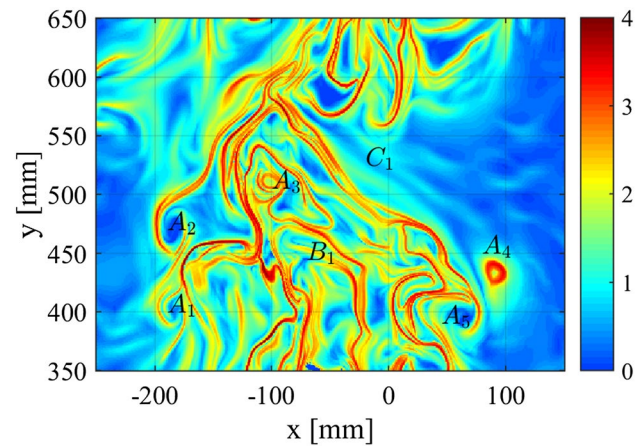


Fig. 19 Lagrangian coherent structures diagnosed from the backward-time FTLE field $\sigma(x, t, t_0)$ computed from the flow map in Fig. 18

allows for the identification of detailed transport patterns and opens the possibility to locate LCSs from the FTLE field and also from more involved LCS methods that rely on accurate trajectory data (Hadjighasem et al. 2016; Haller 2015).

6 Conclusions and outlook

A time-resolved volumetric flow measurement of a pure thermal plume with extended heat source was presented. Helium-filled soap bubbles with a quantified lifetime and intensity loss are used as flow tracers and are illuminated by an array of white high-power LEDs. In the measurement volume of 560 L, up to 275,000 bubbles could be tracked simultaneously using the STB algorithm. To the best knowledge of the authors, this investigation involves the largest number of tracked particles for LPT experiments so far. Evaluations using an updated version of the STB algorithm (Jahn 2017) allowed the processing of time series at even higher particle image densities, tracking up to 430,000 bubbles instantaneously in the present experiment. The results, spatially highly resolved vector volumes of velocity and acceleration, interpolated onto an Eulerian grid using the FlowFit method, show a multitude of well-resolved flow structures with a remarkable coherence in time. We also show that, due to the high spatial resolution, the experimental trajectories can directly be used to compute the flow map, to visualize Lagrangian coherent structures showing the fluid transport during the evolution of the thermal plume.

These achievements are possible mainly due to the high image quality in the experiment, i.e., small uniform particle images. The bubble size distribution is narrow around

the peak value of 300 μm (monodisperse) and all bubbles reflect the light to all cameras with similar intensity. The white, nearly incoherent light produced by the LEDs avoids effects like speckles or interference patterns, leading to temporally consistent particle images. All these aspects are beneficial for a reliable tracking process of STB and allow high particle concentrations of up to 0.1 ppp to be used.

The current study successfully demonstrates a large-volume flow measurement with flow velocities below 1 m/s. It is highly desirable to extend the general setup to higher flow velocities, enabling the operation in typical wind tunnel experiments with applications to boundary layer research, the car industry or sports aerodynamics. The three key factors needing to be addressed for a transfer of the presented measurement technique to low-speed wind tunnels are: (1) HFSB generators with an augmented production rate, i.e., increased number of nozzles, (2) high-speed cameras with a resolution of several megapixels and a frame rate of 1–10 kHz, i.e., data throughput of several Giga-pixels/s, and (3) pulsed collimated high-power LED arrays with a small opening angle of the emitted light. Modern equipment with these properties is available and allows for LPT measurements with high seeding concentration in faster flows. This has been shown in a recent experiment with an impinging jet in the same experimental chamber ($U = 16$ m/s, $V = 13$ L, 10 HFSB nozzles, frame rate 3.9 kHz) (Schanz et al. 2016b) and another still unpublished experiment at DLR Göttingen in a turbulent boundary layer in a wind tunnel ($U = 13$ m/s, $V = 180$ L, 100 HFSB nozzles, frame rate 2 kHz). Further studies report similar developments (Scarano et al. 2015; Caridi et al. 2016; Schneiders et al. 2016).

Acknowledgements We would like to thank Carsten Fuchs, Tobias Kleindienst, Michel Wüstefeld, Janos Agocs and Reinhard Geisler for their indispensable technical support while setting up the experiment in the DLR laboratories. Dirk Michaelis was of great help for image acquisition during the course of the experiment. We also acknowledge the loan of cameras and measurement equipment from LaVision GmbH. We appreciate the manuscript corrections by Walter Beck. Work including the experimental results has partly been funded by the DFG-project *Analyse turbulenter Grenzschichten mit Druckgradient bei großen Reynoldszahlen mit hochauflösenden Vielkameramessverfahren* (Grant Nos. KA 1808/14-1 and SCHR 1165/3-1).

References

- Biwole PH, Yan W, Zhang Y, Roux JJ (2009) A complete 3D particle tracking algorithm and its applications to the indoor airflow study. *Meas Sci Technol* 20:115403
- Bosbach J, Kühn M, Wagner C (2009) Large scale particle image velocimetry with helium filled soap bubbles. *Exp Fluids* 46:539–547
- Brunton SL, Rowley CW (2010) Fast computation of finite-time Lyapunov exponent fields for unsteady flows. *Chaos* 20:017503
- Caridi GCA, Ragni D, Sciacchitano A, Scarano F (2016) HFSB-seeding for large-scale tomographic PIV in wind tunnels. *Exp Fluids* 57:190
- Elsinga GE, Scarano F, Wieneke B, van Oudheusden BW (2006) Tomographic particle image velocimetry. *Exp Fluids* 41:933–947
- Gesemann S, Huhn F, Schanz D, Schröder A (2016) From noisy particle tracks to velocity, acceleration and pressure fields using B-splines and penalties. In: 18th international symposia on applications of laser techniques to fluid mechanics, Lisbon, Portugal
- Gilet T, Scheller T, Reyssat E, Vandewalle N, Dorbolo S (2007) How long will a bubble be? [arXiv:0709.4412](https://arxiv.org/abs/0709.4412)
- Hadjighasem A, Karrasch D, Teramoto H, Haller G (2016) Spectral-clustering approach to Lagrangian vortex detection. *Phys Rev E* 93:063107
- Haller G (2001) Distinguished material surfaces and coherent structures in three-dimensional fluid flows. *Physica D* 149:248–277
- Haller G (2015) Lagrangian coherent structures. *Annu Rev Fluid Mech* 47:137–162
- Hong J, Tolouil M, Chamorro LP, Guala M, Howard K, Riley A, Tucker J, Sotiropoulos F (2014) Natural snowfall reveals large-scale flow structures in the wake of a 2.5-MW wind turbine. *Nat Commun* 5:4216
- Jahn T (2017) Volumetric flow field measurement: an implementation of Shake-The-Box, Master thesis, DLR Göttingen/Georg-August-Universität Göttingen
- Klimas P (1973) Helium bubble survey on an opening parachute flow field. *J Aircr* 10:567–569
- Kühn M, Ehrenfried K, Bosbach J, Wagner C (2011) Large-scale tomographic particle image velocimetry using helium-filled soap bubbles. *Exp Fluids* 50:929–948
- Kundu PK, Cohen IM (2008) *Fluid mechanics*. Academic Press, Elsevier
- La Porta A, Voth GA, Crawford AM, Alexander J, Bodenschatz E (2001) Fluid particle accelerations in fully developed turbulence. *Nature* 409:1017–1019
- Maas HG, Grün A, Papantoniou D (1993) Particle tracking in three dimensional turbulent flows—part I: photogrammetric determination of particle coordinates. *Exp Fluids* 15:133–146
- Malik N, Dracos T, Papantoniou D (1993) Particle tracking in three dimensional turbulent flows—part II: particle tracking. *Exp Fluids* 15:279–294
- Melling A (1997) Tracer particles and seeding for particle image velocimetry. *Meas Sci Technol* 8:1406
- Morton BR, Taylor G, Turner JS (1956) Turbulent gravitational convection from maintained and instantaneous sources. *Proc R Soc A* 234(1196):1–23
- Müller RHG, Flögel H, Schere T, Schaumann O, Markwart M (2000) Investigation of large scale low speed air conditioning flow using PIV. In: 9th international symposium on flow visualization, Edinburgh, UK
- Okuno Y, Fukuda T, Miwata Y, Kobayashi T (1993) Development of three dimensional air flow measuring method using soap bubbles. *JSAE Rev* 14:50–55
- Peacock T, Dabiri J (2010) Introduction to focus issue: Lagrangian coherent structures. *Chaos* 20:017501
- Peacock T, Froyland G, Haller G (2015) Introduction to focus issue: objective detection of coherent structures. *Chaos* 25:087201
- Pham MV, Plourde F, Kim SD (2005) Three-dimensional characterization of a pure thermal plume. *J Heat Transf* 127:624–636
- Plourde F, Pham MV, Kim SD, Balachandrar S (2008) Direct numerical simulations of a rapidly expanding thermal plume: structure and entrainment interaction. *J Fluid Mech* 604:99–123
- Pounder E (1956) Parachute inflation process Wind-Tunnel Study, WADC Technical report 56-391, Equipment Laboratory, Wright Patterson Air Force Base, Ohio, USA, pp 17–18

- Raben G, Ross SD, Vlachos PP (2014) Computation of finite-time Lyapunov exponents from time-resolved particle image velocimetry data. *Exp Fluids* 55:1638
- Rosi GA, Sherry M, Kinzel M, Rival DE (2014) Characterizing the lower log region of the atmospheric surface layer via large-scale particle tracking velocimetry. *Exp Fluids* 55:1736
- Rosi GA, Walker AM, Rival D (2015) Lagrangian coherent structure identification using a Voronoi tessellation-based networking algorithm. *Exp Fluids* 56:189
- Scarano F, Ghaemi S, Caridi G, Bosbach J, Dierksheide U, Sciacchitano A (2015) On the use of helium-filled soap bubbles for large-scale tomographic PIV wind tunnel experiments. *Exp Fluids* 311(56):42
- Schanz D, Gesemann S, Schröder A, Wieneke B, Novara M (2013a) Non-uniform optical transfer functions in particle imaging: calibration and application to tomographic reconstruction. *Meas Sci Technol* 24:024009
- Schanz D, Schröder A, Gesemann S, Michaelis D, Wieneke B (2013b) Shake-the-Box: a highly efficient and accurate Tomographic Particle Tracking Velocimetry (TOMO-PTV) method using prediction of particle position. In: 10th international symposium on particle image velocimetry—PIV13, Delft, The Netherlands, July 1–3
- Schanz D, Schröder A, Gesemann S (2014) Shake-the-Box—a 4D PTV algorithm: accurate and ghostless reconstruction of Lagrangian tracks in densely seeded flows. In: 17th international symposium on applications of laser techniques to fluid mechanics, Lisbon, Portugal, July 07–10
- Schanz D, Schröder A, Gesemann S (2016a) Shake-The-Box: Lagrangian particle tracking at high particle image densities. *Exp Fluids* 57:70
- Schanz D, Huhn F, Gesemann S, Dierksheide U, van de Meerendonk R, Manovski P, Schröder A (2016b) Towards high-resolution 3D flow field measurements at cubic meter scales. In: 18th international symposium on applications of laser techniques to fluid mechanics, Lisbon, Portugal
- Schneiders JFG, Caridi GCA, Sciacchitano A, Scarano F (2016) Large-scale volumetric pressure from tomographic PTV with HFSB tracers. *Exp Fluids* 57:164
- Tobin ST, Meagher AJ, Bulfin B, Möbius M, Hutzler S (2011) A public study of the lifetime distribution of soap films. *Am J Phys* 79(819):819–824
- Wieneke B (2008) Volume self-calibration for 3D particle image velocimetry. *Exp Fluids* 45:549–556
- Wieneke B (2013) Iterative reconstruction of volumetric particle distribution. *Meas Sci Technol* 24:024008